PCCP

ROYAL SOCIETY OF CHEMIS

Cite this: DOI: 10.1039/d2cp03389e

Insights into the spontaneous multi-scale supramolecular assembly in an ionic liquid-based extraction system†

Baihua Chen,‡[a] Ce Shi,‡[b] Shijie Xiong,‡[b] Kaige Wu,[b] Yanqiu Yang,[a] Wanjun Mu,[a] Xingliang Li,[a] Yuchuan Yang,[a] Xinghai Shen *[b] and Shuming Peng *[a]

Herein, we report a four-step mechanism for the spontaneous multi-scale supramolecular assembly (MSSA) process in a two-phase system concerning an ionic liquid (IL). The complex ions, elementary building blocks (EBBs), $[EBB]_n$ clusters and macroscopic assembly (MA) sphere are formed step by step. The porous large-sized $[EBB]_n$ clusters in the glassy state can hardly stay in the IL phase and they transfer to the IL–water interface due to both electroneutrality and amphiphilicity. Then, the clusters undergo random collision in the interface driven by the Marangoni effect and capillary force thereafter. Finally, a single MA sphere can be formed owing to supramolecular interactions. To our knowledge, this is the first example realizing spontaneous whole-process supramolecular assembly covering microscopic, mesoscopic and macroscopic scales in extraction systems. The concept of multi-scale selectivity (MSS) is therefore suggested and its mechanism is revealed. The selective separation and solidification of metal ions can be realized in a MSSA-based extraction system depending on MSS. In addition, insights into the physicochemical characteristics of ILs from microscopic, mesoscopic to macroscopic scales are provided, and especially, the solvation effect of ILs on the large-sized clusters leading to the phase-splitting is examined. It is quite important that the polarization of uranyl in its complex, the growing of uranyl clusters in an IL as well as the glassy material of uranyl are investigated systematically on the basis of both experiment and theoretical calculations in this work.

Received 23rd July 2022,
Accepted 29th September 2022

DOI: 10.1039/d2cp03389e

rsc.li/pccp

Introduction

Supramolecular chemistry aims at developing complex chemical systems from components interacting through noncovalent intermolecular forces and self-organization drives towards the systems of increasing complexity, towards more and more complex forms of matter, up to the generation of life and thought.[1–6] Supramolecular self-assembly provides a "bottom-up" strategy to achieve complex species from molecular building blocks.[7,8] It is obvious that the perspectives of supramolecular chemistry should be involved in spontaneous whole processes from microscopic, mesoscopic to macroscopic scales. However, most supramolecular systems investigated at the present time occupy generally the space between the molecular and the nano to meso-scale worlds.[7] And multistep assembling is required for bridging dimensions from the nanoscale to mesoscale, each assembly step setting the stage for the next one in a sequential and/or hierarchical fashion.[6] If the mesoscale structures could further assemble into materials on the macroscopic scale, the spontaneous whole process covering molecular, mesoscopic and macroscopic levels would be realized. We may denominate this process as multi-scale supramolecular assembly (MSSA) for the first time, which is of theoretical and practical importance. In a MSSA process, the key assembling step at the macroscopic level was seldom studied[9] and thus poorly understood. Indeed, supramolecular assembly on macroscopic building blocks with a size over 10 μm has been tried, in which the building blocks were modified with supramolecular interactive groups on the flowable surface.[10–17] Marangoni-driven self-propelled building blocks were designed to achieve spontaneous macroscopic supramolecular assembly and unfortunately the duration of the Marangoni effect was limited despite the great efforts.[18,19] Therefore, to realize a whole-process spontaneous MSSA, the

[a] Institute of Nuclear Physics and Chemistry, China Academy of Engineering Physics, Mianyang, 621999, P. R. China. E-mail: pengshuming@caep.cn
[b] Beijing National Laboratory for Molecular Sciences (BNLMS), Fundamental Science on Radiochemistry and Radiation Chemistry Laboratory, Center for Applied Physics and Technology, College of Chemistry and Molecular Engineering, Peking University, Beijing, 100871, P. R. China. E-mail: xshen@pku.edu.cn

† Electronic supplementary information (ESI) available. See DOI: https://doi.org/10.1039/d2cp03389e

‡ These authors contributed equally to this work.

continuous Marangoni-driven self-propelled process responsible for the macroscopic assembly at the interface is of essential importance.

The supramolecular behaviors in the presence of ionic liquids (ILs) have been investigated intensively because of the coexistence of various non-covalent interactions.[20] Both high separation efficiency and selectivity were observed in the extraction systems with ILs acting as organic solvents and also participating in the formation of supramolecular assemblies.[21–23] Specific supramolecular recognition accounts for the high selectivity in the extraction of a target metal ion. In particular, extensive interests have been focused on the selective extraction of uranium, the actual fuel to the production of nuclear power.[21,24–26] So far, the knowledge concerning the selectivity in an extraction process has not been beyond micro- and meso-scales yet.[27–29] If the MSSA procedure as suggested above could be successfully designed in an extraction system, the function of high selectivity would originate from comprehensive multi-scale effects such as the supramolecular recognition on the microscopic and mesoscopic scales,[12,30] as well as the kinetics controlling on the macroscopic scale depending on the temperature. Evidence is still lacking in the literature that such a multi-scale selectivity (MSS) plays a joint role in the extraction of metal ions. Fortunately, our preliminary results in a recent communication support the novel concepts of MSSA and MSS suggested herein.[31] In addition, the solvation and phase-splitting behaviors of ILs on the multi-scale can offer new insights into the essential physicochemical properties.[32–37] Achieving the MSSA process and thus the opportunity for exploring the characteristics of ILs on multi-scale are greatly demanding.[38–42]

To depict clear pictures of the MSSA and MSS processes, and also to understand the physicochemical characteristics of ILs not only on the microscopic scale but also on mesoscopic and macroscopic scales, we plan to carry out a systematic investigation in this work on the basis of our preliminary results.[31] It is believed that insights into the MSSA and MSS processes will pave the way, to a certain extent, for the development of supramolecular chemistry as a bridge linking the microscopic and macroscopic worlds.

Experimental

Materials

Octyl(phenyl)-*N*,*N*-diisobutylcarbamoylmethylphosphine oxide (CMPO, 98%) was purchased from WuXi AppTec (Shanghai, China). Bis(2-ethylhexyl) phosphate (HDEHP, 98%) and 2-Ethylhexylphosphoric acid mono-2-ethylhexyl ester (P507, 98%) were provided by Lanzhou Institute of Chemical Physics. Ionic liquids $C_2OHmimNTf_2$, $C_2mimNTf_2$, and $C_2NH_2mimNTf_2$ (purities > 99%) were provided by the Lanzhou Institute of Chemical Physics, Chinese Academy of Sciences. The structures of the extractants and ILs are presented in Fig. S1 (ESI†). High purity $UO_2(NO_3)_2{\cdot}6H_2O$ (99.9%) was obtained from Aladdin, China, dried for more than 48 h at 373 K under vacuum conditions, and stored in a desiccator before use. $Al(NO_3)_3{\cdot}9H_2O$ (AR) was procured from Xilong Chemical Co., Ltd (Shantou, Guangdong, China). $LaCl_3{\cdot}6H_2O$ (99.99%), $CeCl_3{\cdot}6H_2O$ (99.99%) and $EuCl_3{\cdot}6H_2O$ (99.99%) were obtained from Shanghai Xianding Biological Science & Technology. $SmCl_3{\cdot}6H_2O$ (99.99%) and $NdCl_3{\cdot}6H_2O$ (99.99%) were received from Shanghai Sun Chemical Technology. $Sr(NO_3)_2$ (AR) was procured from Sinopharm Chemical Reagent Co., Ltd (Beijing, China). 1,2-Dichloroethane, ethanol and acetone were of analytical grade. The $UO_2(CMPO)_3(NO_3)_2$ and the $UO_2(CMPO)_3(NTf_2)_2$ were prepared as previously reported.[31] Ultra-pure water (18.2 MΩ cm) was used throughout the experiments.

Instruments

Fourier transform infrared (FT-IR) spectroscopy was carried out at room temperature on a Fourier transform infrared spectrometer (Nicolet is50, ThermoFisher). The wavenumber ranged from 400 to 4000 cm^{-1}.

UV-vis measurements were obtained on a Hitachi 3010 UV-vis Spectrometer to obtain the spectrum of U-MA, CMPO, $C_2OHmimNTf_2$ and $UO_2(CMPO)_3(NTf_2)_2$ in the ethanol solutions. The concentration of U-MA was 0.3 mM $[UO_2(CMPO)_3]_3[C_2OHmim][NTf_2]_7$. The concentrations of CMPO, $C_2OHmimNTf_2$ and $UO_2(CMPO)_3(NTf_2)_2$ were 2.7, 0.3, and 0.9 mM, respectively.

High-resolution mass spectrometry with electrospray ionization (ESI-HRMS) was performed on a Fourier transform ion cyclotron resonance mass spectrometer, Solarix XR (Bruker, Germany).

Elemental analysis (EA) was performed on an elemental analyzer (vario EL, Elementar Analysensysteme GmbH, Germany) with carbon, oxygen and hydrogen element contents measured.

Dynamic light scatting (DLS) measurements of the ethanol solutions were performed on a Malvern Nano ZS90 instrument (Malvern Instruments, UK) at 298.2 K and at a scattering angle of 90° (wavelength: 633 nm). A He–Ne laser with a power of 4 mW was used as the light source. The Malvern General Purpose method provided by Malvern analyzes the autocorrelation function and calculates the distribution of the diffusion coefficient D of the particles. The diffusion coefficient is converted into an effective hydrodynamic radius R_H by using the Stokes-Einstein equation. The samples were centrifuged under 4000 rpm for 10 minutes and the supernatant was taken for DLS measurement.

For cryo-transmission electron microscopy (cryo-TEM) studies, the U-MA was sliced using an ultramicrotome (Leica EM UC6) at −10 °C and the thin film was about 50 nm thick. The film was put on a lacey carbon film covered copper grid and then was cooled to approximately 90 K by liquid nitrogen. The specimen was inserted into a high tilt liquid nitrogen cryo transfer tomography holder (Gatan-914, America) and transferred to a TEM instrument (JEM-2100, JEOL, Japan). Examinations were carried out at temperatures around −20 °C.

For TEM studies, the samples were prepared by placing a 3 μL droplet of ethanol solution of U-MA onto a copper grid for

5 min and left to dry overnight before imaging. The examinations were carried on the TEM instrument (FEI Tecnai T20, America).

The interfacial tension of the IL–water interface was measured by the pendant-drop method using an Interface Tensiometer, OSA 100 (LAUDA Scientific, Germany). The temperature was controlled by external circulating water.

Methods

Synthesis of ILs. Syntheses of $C_nOHmimNTf_2$ (n = 3, 4)[43] and $C_2FmimNTf_2$[44] were conducted as follows. Under a nitrogen atmosphere, 3-bromo-1-propanol (for $C_3OHmimNTf_2$) and 4-bromo-1-butanol (for $C_4OHmimNTf_2$) were carefully added to an equal amount of 1-methylimidazole in an ice bath. The analogous bromide salts were prepared by reaction for 24 h at room temperature. 2-Fluoro-1-bromoethane (for $C_2FmimNTf_2$) was carefully added to an equal amount of 1-methylimidazole in an ice bath. The bromide salts were prepared by reaction for 24 h at 80 °C. The resulting ILs were washed with ethyl acetate. After the last washing, the remaining ethyl acetate was removed by heating up to 60 °C under vacuum. The final bis(trifluoromethylsulfonyl)imide type ILs were prepared by slowly adding bis(trifluoromethylsulfonyl)imide lithium salt (1.1 mol eq.) to the corresponding bromide in deionized water. After stirring for 24 h, the lower ionic liquid layer was washed with deionized water 5 times to remove any remaining LiBr. The remaining water was removed by heating up to 60 °C under vacuum. $C_3OHmimNTf_2$: ESI-MS: m/z (+): 141.1; m/z (−): 279.9. Elem. Anal. (%) Calcd for $C_9H_{13}F_6N_3O_5S_2$: C, 25.66; H, 3.11; N, 9.97. Found: C, 25.69; H, 3.15; N, 10.15. $C_4OHmimNTf_2$: ESI-MS: m/z (+): 155.1; m/z (−): 279.9. Elem. Anal. (%) Calcd for $C_{10}H_{15}F_6N_3O_5S_2$: C, 27.59; H, 3.47; N, 9.65. Found: C, 27.65; H, 3.51; N, 9.74. $C_2FmimNTf_2$: ESI-MS: m/z (+): 129.1, 538.1; m/z (−): 279.9. Elem. Anal. (%) Calcd for $C_8H_{10}F_7N_3O_4S_2$: C, 23.48; H, 2.46; N, 10.27. Found: C, 23.45; H, 2.44; N, 10.56.

Preparation of MA sphere. For the synthesis and preparation of an MA sphere, we took U-MA from CMPO-$C_2OHmimNTf_2$ system as an example. Working solutions of 60 mM ligand were prepared by dissolving CMPO with the desired weight in $C_2OHmimNTf_2$ using a volumetric flask. Uranium solutions for the extraction experiments were prepared by dissolving weighted $UO_2(NO_3)_2{\cdot}6H_2O$ in certain concentrations of HNO_3 solutions. The exact concentrations of uranium were determined using an inductively coupled plasma-atomic emission spectrometer (ICP-AES, Leeman, USA) with relative standard deviation (RSD) below 5%. An equal volume of 10 mM $UO_2(NO_3)_2$ in 0.1 M HNO_3 and 60 mM CMPO in $C_2OHmimNTf_2$ were mixed in a vial at constant temperature. Several yellow visible spheres appeared momentarily at the IL–water interface. The mixture was left for one week without stirring and the assemblies spontaneously converged into one single MA sphere. The MA sphere was then taken out with a tweezer and placed in a Petri dish for air drying non-structural water and IL remaining on the surface. The distributions of UO_2^{2+} in aqueous phase and IL phase during the MSSA process at different temperatures were determined by ICP-AES and ICP-MS (Element XR, Thermo Fisher Scientific, America) with relative standard deviation (RSD) below 5%. The IL phases were digested using a Microwave Digestion System (Mars6 Xpress, CEM, America) before the measurements.

Separation between UO_2^{2+} and Al^{3+}, Fe^{3+}. The separation between UO_2^{2+} and Al^{3+} was carried out as follows: 10 mM solutions of UO_2^{2+}, Al^{3+} with 0.1 mol L^{-1} nitric acid were prepared respectively. A mixture of 10 mM UO_2^{2+}, Al^{3+} with 0.1 mol L^{-1} nitric acid was also prepared. The exact concentrations of metal ions were determined by ICP-AES and the acidity was determined using a pH meter (Delta 320, Mettler-Toledo, Switzerland). The metal ion solutions were mixed with 60 mM CMPO/$C_2OHmimNTf_2$ solutions and MSSA-based separation experiments lasted for 7 days at different temperatures. The IL and MA phase were digested using a Microwave Digestion System (Mars6 Xpress, CEM, America) before ICP-AES measurement. The separation between UO_2^{2+} and Fe^{3+} was carried out in the same way.

Separation between UO_2^{2+} and Ln^{3+}, Sr^{2+}. The separation between UO_2^{2+} and Ln^{3+}, Sr^{2+} was carried out as follows: 60 mM HDEHP/$C_2OHmimNTf_2$ solution was prepared with $C_2OHmimNTf_2$ balanced with nitric acid, and a certain amount of absolute ethanol was added as the co-solvent in the preparation process. In 2 M, 1 M, 0.7 M, 0.5 M, 0.3 M, 0.1 M and 0.01 M nitric acid, 10 mM solutions of UO_2^{2+}, Ce^{3+}, La^{3+}, Nd^{3+}, Sm^{3+}, Eu^{3+}, Sr^{2+} and Ba^{2+} were prepared respectively. A mixture of 10 mM UO_2^{2+}, Ce^{3+}, La^{3+}, Nd^{3+}, Sm^{3+}, Eu^{3+} and Sr^{2+} in nitric acid with different concentrations were also prepared. Metal ion solutions with different concentrations of nitric acid were mixed with HDEHP/$C_2OHmimNTf_2$ respectively, and MSSA-based separation experiments were carried out at room temperature. The concentrations of metal ions in the aqueous, IL and MA phases were determined by ICP-AES. The analytical sample of the IL phase was prepared in a different way: 0.3 mL content of the IL phase was repeatedly dried with a mixture of concentrated HNO_3/$HClO_4$ (10 mL, 2/1 by volume) in a glass flask three times to destroy the organics. The flask was later heated slowly to 300 °C to vaporize excessive acids. 20 mL of 0.1 M HNO_3 was then added in the flask to dissolve metal ions thoroughly for ICP-AES analysis. The procedure for the preparation of the MA phase analytical sample was almost the same, but with the total dissolution of the entire MA sphere.

Calculation methods. All DFT calculations were carried out in Gaussian 09. D.1.[45] B3LYP[46,47] hybrid functional was used. For the U atom, the Stuttgart pseudopotential and complementary basis set[48–50] were used. For light elements, def2-SVP basis sets were used for optimization while def2-TZVP basis sets were used in RESP charge calculations and electrostatic interaction.[51,52] For geometry optimization, RESP charge calculations of ions and electrostatic interaction, the SMD-GIL method[53] was used. We added diffuse functions of aug-cc-pVDZ[54] to def2-TZVP basis sets for calculations of $[NTf_2]^-$ ion. RESP charge and molecular electrostatic potential were calculated in Multiwfn3.8.[55,56] For electrostatic interaction calculation between $[UO_2(CMPO)_3]^{2+}$ and $[NTf_2]^-$ the DFT-D3 method was used.[57] The molecular electrostatic potential was drawn in

VMD 1.9.3.[58] The molecular simulations were carried out in Gromacs5.0.7.[59] The UFF force field[60] parameters were referred to OBGMX2.0.[61] For all MD simulations, we used the NPT ensemble with a V-rescale thermostat[62] and Parrinello-Rahman barostat[63] at 323 K and 1 atmosphere. Constants for temperature coupling and pressure coupling were 0.1 ps and 2 ps respectively. For van der Waals interaction, we used a cut-off method with 1 nm distance. For electrostatic interaction, we used a Particle-Mesh Ewald method.[64] For the $[UO_2(CMPO)_3]_3[C_2OHmim][NTf_2]_7$ unit, we set a cubic box with 3 nm. For the $[EBB]_5$ cluster, we set a cubic box with 6 nm and we added 200 pairs $[C_2OHmim]^+$ and $[NTf_2]^-$. For the $[EBB]_{20}$ cluster, we set a cubic box with 8 nm. All simulations ran with 1 ns pre-equivalent time and 10 ns equivalent simulation time. The TDDFT calculations were done in ORCA 5.0.2[65] at the level of RIJCOSX[66]/B3LYP/def2-TZVP/SMD[67] with 20 lowest roots solved for $[C_2OHmim]^+$ in ethanol. For calculation about $[C_2OHmim]^+$ in a micro environment of EBB, the ma-def2-TZVP basis sets,[68] DFT-D3 and SMD-GIL were used to solve the 20 lowest roots. For the $[Al(CMPO)_3]_3[C_2OHmim][NTf_2]_{10}$ unit, we set a cubic box with 3 nm. For Al-EBB, we set a cubic box with 6 nm and we added 200 pairs $[C_2OHmim]^+$ and $[NTf_2]^-$ to calculate solvation energy. For the $[Al\text{-}EBB]_5$ cluster, we set a cubic box with 6 nm to calculate the binding energy. The calculation methods of Fe-MSSA were the same as that of Al-MSSA. The EBB calculations of the $C_2mimNTf_2$ and $C_3OHmimNTf_2$ based system were similar to that of the $C_2OHmimNTf_2$ based system.

Results and discussion

Mechanism of the MSSA process

When mixing the $C_2OHmimNTf_2$ bearing CMPO with the aqueous solution of uranyl in the presence of HNO_3, a single MA sphere (abbreviated as U-MA) is formed at the interface (Fig. S2a, ESI†). The preliminary mechanism was speculated in our previous work.[31] We further propose herein a four-step MSSA mechanism as illustrated in Scheme 1 by structural characterization and theoretical calculation. The four level structures, *i.e.* complex ions, elementary building blocks (EBBs), $[EBB]_n$ clusters and MA sphere, are formed step by step. The first step includes the cation exchange and formation of complex ions. The second step is the formation of EBBs. The third step is the formation of $[EBB]_n$ clusters, which move from IL to the interface. The fourth step is the macroscopic supramolecular assembly in the interface.

Step 1: cation exchange and formation of complex ions. The distribution of UO_2^{2+} in the aqueous phase declines sharply, while that in the IL phase is enhanced at first and then goes down in the initial stage of the MSSA process (Fig. S3, ESI†) and then both of them reach a plateau. This result indicates that uranyl ions can be extracted to the IL phase and thus confirms the cation exchange in the first step of the MSSA process. The characteristics of the first level structure $[UO_2(CMPO)_3]^{2+}$ should be clarified.[31,69] FT-IR spectra of U-MA and $UO_2(CMPO)_3(NO_3)_2$ were measured,[31] in which the C═O absorption peaks of both U-MA and $UO_2(CMPO)_3(NO_3)_2$ split at 1613 cm^{-1}. For comparison, the FT-IR spectra of Al-MA, Fe-MA and CMPO are recorded in this work (see Fig. 1a), where no similar splits can be observed. Obviously, it is the special coordination pattern in $[UO_2(CMPO)_3]^{2+}$ that causes the splits as mentioned above. We believe that not all C═O bonds in three CMPO molecules are involved in the coordination with a uranyl ion. By contrast, the stretching vibrational absorption of P═O moves from 1177 cm^{-1} in CMPO (see Fig. 1a) to 1131 cm^{-1} in $[UO_2(CMPO)_3]^{2+}$ as reported previously without splitting.[31] Considering that the phosphoric O-donor is of stronger basicity than the carbonyl O-donor,[70,71] we believe that the three P═O bonds in $[UO_2(CMPO)_3]^{2+}$ are all involved in the coordination with uranyl while the three C═O bonds are not.

We used density functional theory (DFT) to reveal the reasonable structural characteristics of $[UO_2(CMPO)_3]^{2+}$ in the IL phase.

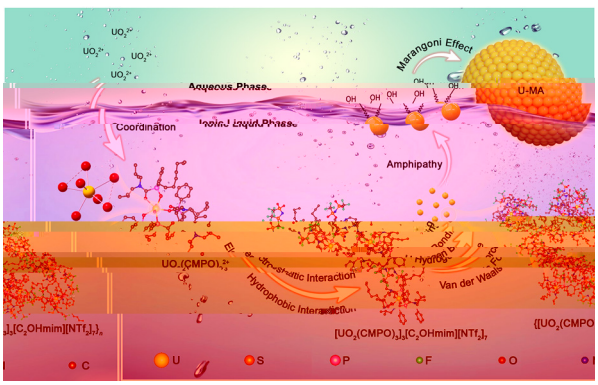

Scheme 1 The four-step formation mechanism for the MSSA process.

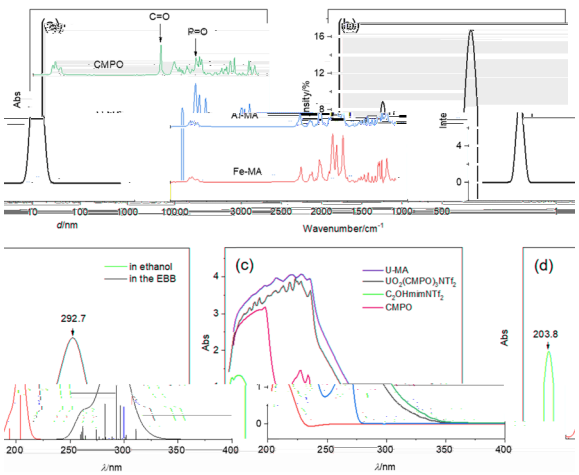

Fig. 1 The spectroscopic analyses of the MA sphere. (a) FT-IR spectra of CMPO, Al-MA and Fe-MA. (b) DLS results of U-MA dissolved in ethanol. The concentration of U-MA is expressed by 2 mM $[UO_2(CMPO)_3]_3[C_2OHmim][NTf_2]_7$. (c) UV-Vis spectra of U-MA, CMPO, IL and $UO_2(CMPO)_3(NTf_2)_2$ dissolved in ethanol. The concentration of CMPO, IL and $UO_2(CMPO)_3(NTf_2)_2$ is 0.3, 2.7, and 0.9 mM, respectively. The concentration of U-MA is expressed by 0.3 mM $[UO_2(CMPO)_3]_3[C_2OHmim][NTf_2]_7$. (d) Calculated UV-Vis spectra for $[C_2OHmim]^+$ ions in ethanol and in EBB. The perpendicular lines were obtained by TDDFT calculation and the curves were obtained by widening of lines.

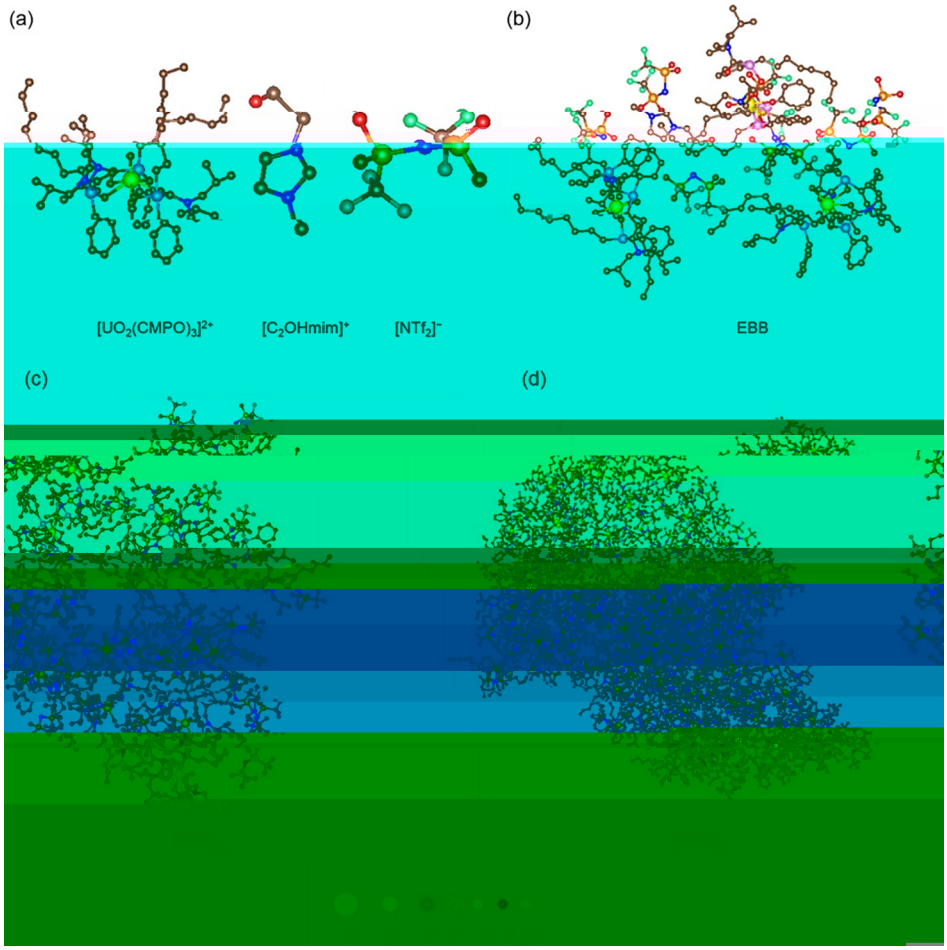

Fig. 2 Theoretical calculation on various structures. (a) $[UO_2(CMPO)_3]^{2+}$, $[C_2OHmim]^+$ and $[NTf_2]^-$. Uranyl is penta-coordinated and one carbonyl in CMPO is not coordinated to uranyl. (b) $[UO_2(CMPO)_3]_3[C_2OHmim][NTf_2]_7$ unit (EBB). (c) $[EBB]_5$ cluster. (d) $[EBB]_{20}$ cluster.

Tetra-coordinated, penta-coordinated and hexa-coordinated initial structures were constructed. The optimized penta-coordinated structure is the ground state. We can see clearly from Fig. 2a that uranyl is coordinated by five O atoms from three CMPO molecules. One carbonyl O atom is not coordinated with the U atom. This coordinate configuration means that the carbonyls in $[UO_2(CMPO)_3]^{2+}$ are not equivalent, in agreement with the FT-IR results mentioned above. In this asymmetric coordination, the uranyl ion deforms with a distorted angle about 4.0°. The bond length between the U atom and different O atoms are shown in Table S1 (ESI†). The distances between the U atom and terminal O atoms are a little longer than those of uranyl in vacuum. We then calculated the restrained electrostatic potential (RESP) charges[72] of both UO_2^{2+} in vacuum and $[UO_2(CMPO)_3]^{2+}$ in $C_2OHmimNTf_2$. The charges of UO_2^{2+} and its U atom and terminal O atoms in vacuum are +2.000, +2.610, and −0.3050, while those of $[UO_2(CMPO)_3]^{2+}$ in $C_2OHmimNTf_2$ are +0.4492, +1.401, and −0.4579, respectively. The more negative charge of terminal O atoms in uranyl coordinated to CMPO strongly suggests that uranyl is polarized. This kind of polarization has been observed in the literature.[73] The decreased positive charge on uranyl in $[UO_2(CMPO)_3]^{2+}$ indicates that the positive charge transfers from uranyl to CMPO. The red cover of $[UO_2(CMPO)_3]^{2+}$ in Fig. S4 (ESI†) means the positive surficial electrostatic potential and the deeper red colour indicates the more positive electrostatic potential. The average charge for C8 chains of CMPO is +0.1424 when CMPO coordinates to uranyl, while that of free CMPO is +0.1148. The increased positive charge on the C8 chain provides a more stable interaction with $[NTf_2]^-$.

Different extractants were tried. Besides CMPO, we found that 2-ethylhexylphosphoric acid mono-2-ethylhexyl ester (P507) and bis(2-ethylhexyl) phosphate (HDEHP) could also form a MA sphere with UO_2^{2+} in the IL–water interface. It is noted that the extractants are bidentate ligands with a large steric hindrance. Similar penta-coordination can also be found in the complex ions between uranyl and HDEHP, P507 ligands (Fig. S3 and Table S1, ESI†). The complex ions formed by HDEHP or P507 with uranyl would have different coordination models and charge dispersion due to their structural changes at different acidities. Therefore, the formation of the MA sphere would be influenced by the acidity.

Step 2: formation of EBB. Whether EBBs do exist in the MSSA process is still unclear, although the chemical composition of the MA sphere was demonstrated to be

$[UO_2(CMPO)_3]_3[C_2OHmim][NTf_2]_7$.[31] In order to figure out the existence of EBBs in the U-MSSA process, we measured the size distribution by DLS after dissolving U-MA in ethanol. Fig. 1b shows two peaks at about 2.5 nm and 160 nm, respectively. The peak at 2.5 nm can be ascribed to the size of EBB, *i.e.* the second level structure. The $[UO_2(CMPO)_3]^{2+}$ complexes interact with the cation and anion of the IL leading to the formation of EBBs, which is regarded as the second step of the MSSA process. The EBBs can further aggregate to a cluster with a larger size, corresponding to the peak at 160 nm.

We used a force field to search the structure of EBB. From simulations, it could be concluded that there does exist a unique unit (Fig. 2b) constructed by three $[UO_2(CMPO)_3]^{2+}$, one $[C_2OHmim]^+$ and seven $[NTf_2]^-$ ions, which is in good agreement with the chemical composition.[31] The calculated diameter of the $[UO_2(CMPO)_3]_3[C_2OHmim][NTf_2]_7$ unit is 2.3 nm, which agrees with the DLS result, and thus the unit is identified as the EBB. We used DFT to investigate the interaction between $[UO_2(CMPO)_3]^{2+}$ and $[NTf_2]^-$. The binding energy between them is −82.4 kJ mol^{-1} due to the electrostatic interaction and hydrophobic interaction. The $[C_2OHmim]^+$ is captured by *n*-octyl groups, benzene rings of $[UO_2(CMPO)_3]^{2+}$ ions and $[NTf_2]^-$ ions in EBB (Fig. 3a). The cavity capturing $[C_2OHmim]^+$ ion has a diameter of about 972 pm and the length of $[C_2OHmim]^+$ is 839 pm (Table S2, ESI†). Furthermore, the OH group in the $[C_2OHmim]^+$ ion can form hydrogen bonds with the terminal O atoms of polarized uranyl and $[NTf_2]^-$ ions (Fig. 3b), which enhances the stability of EBB. To confirm the existence of EBB, we further monitored the microenvironment changes of $[C_2OHmim]^+$ by UV-Vis analyses.[74,75] As shown in Fig. 1c, the characteristic absorption peak in 210 nm of the imidazolium in $C_2OHmimNTf_2$ disappears in the spectra of U-MA, indicating that the microenvironment of $[C_2OHmim]^+$ changes. We also used Time Dependent Density Functional Theory (TDDFT) to calculate the UV-Vis spectra (Fig. 1d) of $[C_2OHmim]^+$ both in the microenvironment from EBB (Fig. 3c) and in ethanol. The calculation results show that the characteristic absorption of $[C_2OHmim]^+$ in ethanol is at 203.8 nm and it increases to 292.7 nm when trapped in EBB, which is in agreement with the experimental results.

The hydroxyl-functionalized IL $C_2OHmimNTf_2$ was the first IL found to form U-MA[31] and similar ILs, $C_nOHmimNTf_2$ (n = 3,4), were also tried to participate in the MSSA process in this work. It took a longer time to form U-MA in the $C_3OHmimNTf_2$ system, whereas the U-MA could not be formed in the $C_4OHmimNTf_2$ system. This is due to the fact that the matching degree of the $[C_nOHmim]^+$ in EBBs becomes lower as the n rises. As listed in Table S2 (ESI†), the diameters of EBB and the cavity capturing imidazolium cation in the $C_3OHmimNTf_2$ system are 3.0 nm and 1198 pm, respectively, while the length of $[C_3OHmim]^+$ is 965 pm. It is inferred that the EBB in the $C_3OHmimNTf_2$ system is loose and unstable compared with the $C_2OHmimNTf_2$ system. For the $C_4OHmimNTf_2$ based system, the matching degree might be too low to form EBB. In addition, methylimidazole cations modified with different functional groups could also make much difference in various steps of the MSSA process. In the $C_2mimNTf_2$ based system, the occurrence of U-MA was not observed, although the EBB with the diameter of 2.8 nm could be formed according to the calculation (see Table S2, ESI†). This indicates that the OH group of the IL is quite important in the MSSA process. We also tried $C_2NH_2mimNTf_2$ and $C_2FmimNTf_2$ as the IL phase, between which only $C_2FmimNTf_2$ could achieve the formation of U-MA. The results further verified the importance of electrostatic interaction. $[C_2NH_2mim]^+$ is more electrically positive than $[C_2Fmim]^+$ and $[C_2OHmim]^+$ because the amino group would more likely act as NH_3^+ in the highly acidic environment and thus increases the repulsion from the electrically positive C8 chains of CMPO. It is difficult for EBB to be formed in the $C_2NH_2mimNTf_2$ system.

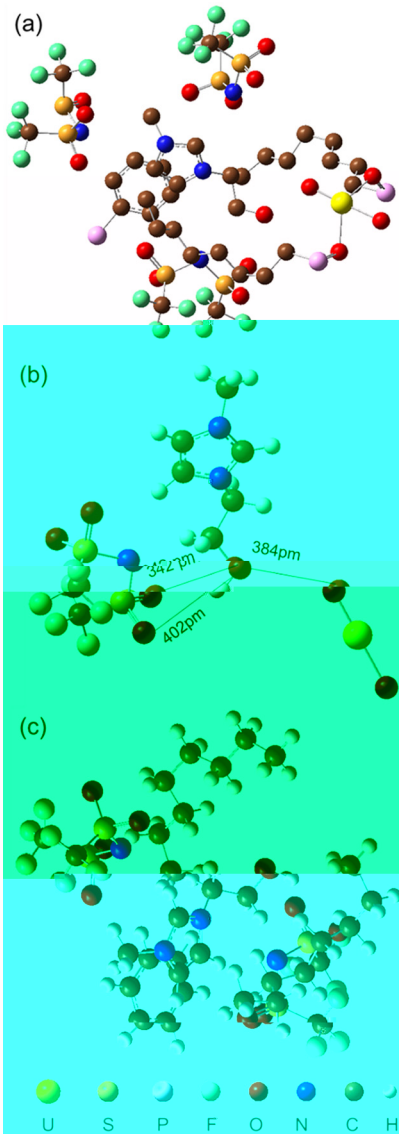

Fig. 3 (a) The inclusion structure formed by $[NTf_2]^-$ and $[UO_2(CMPO)_3]^{2+}$ capturing an $[C_2OHmim]^+$ ion. (b) Hydrogen bond among $[C_2OHmim]^+$ ion, $[NTf_2]^-$ ion and $[UO_2(CMPO)_3]^{2+}$. CMPO molecules are omitted for clarity. (c) The local environment used in the calculation containing an $[C_2OHmim]^+$ ion intercepted from EBB and adjusted by H atoms.

Step 3: formation of $[EBB]_n$ clusters and transferring from the IL phase to the interface. We used a force field to research the third step and the third level structure of the MSSA process. The clusters containing five and twenty EBBs as models for the mesoscopic third level structure were calculated, respectively. The driving force for the formation of the third level structure was investigated. The diameter of the $[EBB]_5$ cluster shown in Fig. 2c is about 5 nm, while that of the $[EBB]_{20}$ cluster in Fig. 2d is around 10 nm. The $[EBB]_5$ and the $[EBB]_{20}$ clusters exhibit similar structural characteristics. They are not uniform and have some cavities in the interior. For the $[EBB]_{20}$ cluster on the mesoscopic scale, we calculated the partial numerical density of atoms along three directions and the radial distribution function (RDF) to describe the structural property of the third level structure. Fig. 4a–c show the partial numerical density along three directions of space. The non-uniform partial numerical density means that the cluster is heterogeneous. This suggests that the atoms are distributed unevenly in the $[EBB]_{20}$ cluster. The empties within the $[EBB]_{20}$ cluster are an indication that there are some cavities in the third level structure. Cryo-TEM of the slice from U-MA shown in Fig. 5a exhibits the section image *in situ* and the heterogeneity on the mesoscale can be observed. One can also see the cavities in the TEM of U-MA dissolved in ethanol (Fig. 5b), which confirms the uneven distribution of the aggregates of EBBs. The fact that the radial distribution function $g(r)$ shown in Fig. 4d trends to 1 with little fluctuations along with the distance increasing further reveals the nature of the MA sphere as a glassy state matter.[76]

We calculated the binding energy per EBB ($E_{b,U}$) of the process that 20 EBBs assemble to the $[EBB]_{20}$ cluster. It is -280 kJ mol^{-1} (Table 1). The contributions of the short-range van der Waals force and electrostatic interaction are -196 and -31.6 kJ mol^{-1}, respectively, while those of the long-range are -44.5 and -2.1 kJ mol^{-1}. Due to the charge screening effect within an electroneutral EBB, the electrostatic interaction between opposite charges belonging to different EBBs is much weaker than van der Waals forces. Furthermore, we calculated the solvation energy $E_{s,U}$ of EBB. It is -82.2 kJ mol^{-1} (see Table 1). The van der Waals force contributes the main part of $E_{s,U}$ because polar groups including OH interact with each other within an electroneutral EBB. The total electrostatic interaction part of $E_{s,U}$ is positive, indicating that there exists electrostatic repulsion between EBBs and IL. This is because the electroneutral EBB occupies the space in IL and breaks its microstructure. In addition, the formation energy ΔE_U ($E_{b,U}$ minus $E_{s,U}$) in the $C_2OHmimNTf_2$-based system is

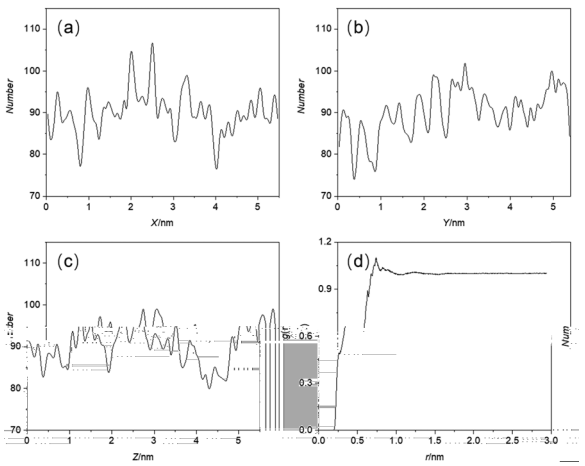

Fig. 4 The partial numerical density and radial distribution function for the $[EBB]_{20}$ cluster. (a–c) Partial numerical density for the $[EBB]_{20}$ cluster along the *X* direction (a), *Y* direction (b) and *Z* direction (c). It is clear that the atoms are in heterogeneous distribution. (d) The radial distribution function (RDF) $g(r)$ of the $[EBB]_{20}$ cluster.

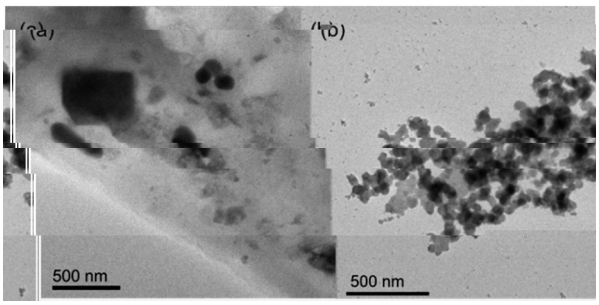

Fig. 5 The morphological characterizations. (a) The *situ* cryo-TEM image of ultrathin sectioning of the U-MA. (b) The TEM image of the U-MA in ethanol solution.

Table 1 Contribution of van der Waals forces and electrostatic interaction to binding energy $E_{b,i}$[a], solvation energy $E_{s,i}$[a] and formation energy ΔE_i[c] (i = U, Al, Fe)

	van der Waals force		Electrostatic interaction			
	Short-range	Long-range	Short-range	Long-range	Others[b]	Sum
T = 323 K $C_2OHmimNTf_2$						
$E_{b,U}$	−196	−44.5	−31.6	−2.1	−5.8	−280
$E_{s,U}$	−70.0	−14.6	14.8	−8.2	−4.2	−82.2
ΔE_U						−198
$E_{b,Al}$	−102	−43.6	56.6	6.4	−55.4	−138
$E_{s,Al}$	−34.2	−23.2	−42.0	−32.1	2.5	−129
ΔE_{Al}						−9.0
$E_{b,Fe}$	−16.0	−13.4	1.6	−6.2	5.4	−28.6
$E_{s,Fe}$	14.6	−18.0	38.2	−43.1	3.3	−5.0
ΔE_{Fe}						−23.6
T = 298 K $C_2OHmimNTf_2$						
$E_{b,U}$	−183	−49.1	26.5	4.48	26.1	−175
$E_{s,U}$	−38.6	−4.60	−29.8	−22.2	−31.8	−127
ΔE_U						−48
T = 323 K $C_2mimNTf_2$						
$E_{b,U}$	−8.8	13.5	−57.3	−13.9	−40.5	−107
$E_{s,U}$	−71.6	−10.6	−94.0	7.4	−50.2	−219
ΔE_U						112
T = 277 K $C_2OHmimNTf_2$						
$E_{b,Al}$	−112	−36.0	20.8	12.8	19.4	−95.0
$E_{s,Al}$	−47.0	−23.0	90.0	−29.0	−78.0	−87.0
ΔE_{Al}						−8.0

[a] kJ mol^{-1}. [b] The energy resulting from bond vibrations, angle bending, dihedral terms, potential and kinetics. [c] $\Delta E = E_b - E_s$. The E_s is the energy of the process that an isolated EBB solves in the IL phase. The E_b is the binding energy averaged per EBB of the process that n EBB at the isolation state assemble to the $[EBB]_n$ cluster. The ΔE is the formation energy of the process that EBBs solved in the IL phase assemble to $[EBB]_n$ clusters.

-198 kJ mol^{-1} (Table 1), indicating that the EBBs can assemble into $[EBB]_n$ clusters spontaneously in the IL phase. $[EBB]_n$ clusters occupy more space of IL and get stronger electrostatic repulsion with IL. When the $[EBB]_n$ clusters grow to be large enough, they can stay in the IL phase no longer. Instead, the large-sized $[EBB]_n$ clusters prefer to transfer to the IL–water interface due to their porous electroneutral structures. The multi-level driving forces prompt the glassy state matter to grow in ionic liquid. We also modelled the system of uranyl at 298 K and the ΔE_U was estimated to be -48 kJ mol^{-1} (Table 1). For comparison, we calculated ΔE_U in C_2mimNTf$_2$ at 323 K (Table 1). The formation energy is 112 kJ mol^{-1} suggesting that EBBs cannot form large-sized $[EBB]_n$ clusters and thus rationalizing the absence of the U-MA sphere in the C_2mimNTf$_2$ based system.

Step 4: macroscopic supramolecular assembly in the interface. The fourth step of the MSSA process is the macroscopic supramolecular assembly in the interface. Considering the size, the formed MA sphere is actually across the IL–water interface. This final step of the MSSA process should be driven by the Marangoni effect. So far, the Marangoni effect has been widely used for continuous self-propulsion of floating machines,[77–79] but the limited duration of the Marangoni effect has been a problem for the application of macroscopic supramolecular assembly.[18,19] For instance, Shi's group designed macroscopic polydimethylsiloxane building blocks in the air-water interface. The building blocks could release surfactants in the interface leading to the occurrence of the concentration gradient and thus the Marangoni effect. However, the fast saturation of surfactants on the surface greatly limited the duration of the Marangoni effect.[18,19]

The progress in research of the solute-induced Marangoni effect occurring in the liquid-liquid extraction was reviewed.[80] The inhomogeneity of the solute can generate a local interfacial tension gradient which tends to trigger the Marangoni effect. The accompanied shearing convection of the bulk flow parallel to the interface might happen and result in the so-called Marangoni convection. Generally speaking, the theory for the Marangoni effect in the liquid-liquid extraction process is still premature and the essence of the interphase mass transfer has not been fully revealed.[80] In the present work, the continuous transferring of $[EBB]_n$ clusters from the IL phase to the interface cause a great disturbance on the local distribution of the surface-active IL (see the interfacial tension values in Fig. S6, ESI†) in the interface. In this case, both the concentration gradient and interfacial tension gradient are large enough to make the Marangoni effect visible and durative. The spontaneous and continuous Marangoni effect can accompany the whole MSSA process. When the $[EBB]_n$ clusters approach within a critical distance, capillary forces begin to work for the minimization of the interfacial free energy of the system by eliminating the curved menisci.[18,19,81] Within the scope of the molecular recognition, the van der Waals force plays a role in the healing of $[EBB]_n$ clusters. The clusters can grow up to macroscopic scales and eventually assemble into one single MA.

The curvature effect in ref. 82–87 was exhibited in the mesoscopic interface in microemulsions, while the Marangoni effect and capillary interaction mentioned in this work corresponded to the macroscopic supramolecular assembly in the IL–water interface. The coarse-grain model was adopted to simulate mesoscopic clusters in the extraction system and was successfully compatible with experiments.[82–87] In this work, more details of the MSSA system were described by full-atom MD to simulate the formation of EBB and $[EBB]_n$ clusters. The results of macroscopic calculation[88] suggested that the coarse-grain model might be a suitable method to simulate the macroscopic supramolecular assembly driven by the Marangoni effect and capillary interaction. However, the specific approach using the coarse-grain model should be based on a set of parameters obtained from experiments. This kind of investigation will be carried out in our future work, which can help understand the mechanism of the macroscopic supramolecular assembly driven by the Marangoni effect and capillary interaction.

According to the above results, the detailed four-step MSSA mechanism for the CMPO-C_2OHmimNTf$_2$/$UO_2(NO_3)_2$ system is illustrated in Scheme 1 and the equilibria corresponding to four steps are given as follows:

$$3\mathrm{CMPO}_{[IL]} + 2\mathrm{C_2OHmimNTf_2}_{[IL]} + {\mathrm{UO_2}^{2+}}_{[aq]} \rightleftharpoons [\mathrm{UO_2(CMPO)_3}][\mathrm{NTf_2}]_{2\,[IL]} + 2{\mathrm{C_2OHmim}^{+}}_{[aq]} \quad (1)$$

$$3[\mathrm{UO_2(CMPO)_3}][\mathrm{NTf_2}]_{2\,[IL]} + \mathrm{C_2OHmimNTf_2}_{[IL]} \rightleftharpoons \mathrm{EBB}_{[IL]} \quad (2)$$

$$n\mathrm{EBB}_{[IL]} \rightleftharpoons [\mathrm{EBB}]_{n\,[IL]} \rightleftharpoons [\mathrm{EBB}]_n\,[\mathrm{interface}] \quad (3)$$

$$m[\mathrm{EBB}]_n\,[\mathrm{interface}] \rightleftharpoons \mathrm{U\text{-}MA[interface]} \quad (4)$$

The four-step mechanism and the corresponding equilibria should also apply for the MSSA processes of other systems, although the four-level structures may not be exactly the same.

Mechanism of MSS and its application

It is well known that the selectivity in solvent extraction mainly originates from the difference in the coordination effect between metal ions and ligands on the microscale.[27–29] The MSSA process, however, provides an opportunity to realize the selectivity not only on the microscale but also on multi-scale effects.

Selectivity on the microscale. As mentioned above, the formation of a MA sphere would be influenced by the acidity with HDEHP as the extractant. La^{3+}, Ce^{3+}, Nd^{3+}, Sm^{3+}, Eu^{3+} and other lanthanide ions exhibit different behaviors at different acidities in the HDEHP/C_2OHmimNTf$_2$ system (Fig. S7, ESI†). All of them remain in the aqueous phase when the concentration of HNO_3 is higher than 1 M. They begin to form a MA sphere when the concentration of HNO_3 is less than 1 M and the extraction efficiency of the MA phase increases with the decrease of acidity. The weakened deprotonation of HDEHP at a high concentration of HNO_3 makes the coordination between Ln^{3+} and HDEHP rarely occur.[89] On the contrary, HDEHP can coordinate with UO_2^{2+} over this range of acidity.[90] Therefore,

UO_2^{2+}

MA sphere) formed step by step were characterized and particularly, $[UO_2(CMPO)_3]_3[C_2OHmim][NTf_2]_7$ units were confirmed to act as the stable EBBs. Second, the concept of MSS covering microscopic, mesoscopic and macroscopic scales was suggested for the extraction of metal ions. The separation between UO_2^{2+} and Al^{3+} with high selectivity strongly supported the importance of MSS. Besides MSS, the remarkable discrimination on uranyl ions should also originate from the pH effect and polarization of uranyl ions. Third, the Marangoni effect and capillary forces were suggested to drive the discrete $[EBB]_n$ clusters assembling into a single MA sphere in the interface. The continuous and uninterrupted Marangoni effect along with the macroscopic supramolecular assembly process is realized. Finally, from multi-scale calculations, it was found that the uranyl was polarized by ligands, which could form hydrogen bonds with $[C_2OHmim]^+$ promoting the stability of EBB. The continuously growing $[EBB]_n$ clusters in a porous glassy state could hardly stay in the IL phase due to their electroneutrality as well as amphiphilicity and they migrated to the IL–water interface. The calculations on the solvation energy and the binding energy of EBB also revealed a route for the glassy state matter to grow in the IL phase. Therefore, the ILs have been examined not only on microscopic and mesoscopic scales, but also on the macroscopic scale in this work.

To our knowledge, this is the first example realizing whole-process spontaneous supramolecular assembly covering molecular, mesoscopic and macroscopic scales in extraction systems. It is believed that insights into the continuous and uninterrupted Marangoni effect, and the spontaneous MSSA and MSS process can pave the way for the development of supramolecular chemistry as a bridge linking the microscopic and macroscopic worlds. Hopefully, functionalized and even intellectualized MA spheres could be formed spontaneously by an elaborate design.

Author contributions

B. C., C. S. and S. X. contributed equally to this work. B. C., X. S, and S. P. initiated the study, and X. S. and S. P. guided the academic research as joint corresponding authors. C. S, S. X., K. W. and X. S. studied the assembly mechanism by experimental characterization and theoretical calculation. B. C., Y. Y. (Yanqiu Yang), W. M., X. L., Y. Y. (Yuchuan Yang) and S. P. carriedYa-5Tm[(B.)Kihe

27 T. H. Ibrahim, *Sep. Sci. Technol.*, 2011, **46**, 2157–2166.
28 P. Guilbaud and T. Zemb, *Curr. Opin. Colloid Interface Sci.*, 2015, **20**, 71–77.
29 Y. Tian, X. Gao, W. Hong, M. Du, P. Pan, J. Z. Sun, Z. L. Wu and Q. Zheng, *Langmuir*, 2018, **34**, 12310–12317.
30 S. Badaire, C. Cottin-Bizonne, J. W. Woody, A. Yang and A. D. Stroock, *J. Am. Chem. Soc.*, 2007, **129**, 40–41.
31 B. Chen, K. Wu, Y. Yang, N. Wang, Y. Liu, S. Hu, J. Wang, J. Wen, S. Hu, Q. Chen, X. Shen and S. Peng, *Chem. Commun.*, 2019, **55**, 6894–6897.
32 C. Hardacre, J. D. Holbrey, M. Nieuwenhuyzen and T. G. A. Youngs, *Acc. Chem. Res.*, 2007, **40**, 1146–1155.
33 E. W. Castner, Jr., J. F. Wishart and H. Shirota, *Acc. Chem. Res.*, 2007, **40**, 1217–1227.
34 C. H. C. Janssen, N. A. Macias-Ruvalcaba, M. Aguilar-Martinez and M. N. Kobrak, *Int. Rev. Phys. Chem.*, 2015, **34**, 591–622.
35 K. Ueno, *Polym. J.*, 2018, **50**, 951–958.
36 S. Liu, M. Walton, N. V. Tarakina and P. Akcora, *J. Phys. Chem. B*, 2020, **124**, 4843–4850.
37 Y. Li, J. J. Wang, X. M. Liu and S. J. Zhang, *Chem. Sci.*, 2018, **9**, 4027–4043.
38 W. Ge, F. G. Chen, J. Gao, S. Q. Gao, J. Huang, X. X. Liu, Y. Ren, Q. C. Sun, L. M. Wang, W. Wang, N. Yang, J. Y. Zhang, H. Zhao, G. Z. Zhou and J. H. Li, *Chem. Eng. Sci.*, 2007, **62**, 3346–3377.
39 J. H. Li, W. Ge, W. Wang, N. Yang and W. L. Huang, *Curr. Opin. Chem. Eng.*, 2016, **13**, 10–23.
40 K. Dong, X. Liu, H. Dong, X. Zhang and S. Zhang, *Chem. Rev.*, 2017, **117**, 6636–6695.
41 X. M. Liu, X. Q. Yao, Y. L. Wang and S. J. Zhang, *Particuology*, 2020, **48**, 55–64.
42 Y. Wang, H. He, C. Wang, Y. Lu, K. Dong, F. Huo and S. Zhang, *JACS Au*, 2022, **2**, 543–561.
43 K. Shimojo, K. Nakashima, N. Kamiya and M. Goto, *Biomacromolecules*, 2006, **7**, 2–5.
44 Y. Gao and J. M. Shreeve, *Synthesis*, 2004, 1072–1082.
45 M. J. Frisch, G. W. Trucks, H. B. Schlegel, G. E. Scuseria, M. A. Robb, J. R. Cheeseman, G. Scalmani, V. Barone, B. Mennucci, G. A. Petersson, H. Nakatsuji, M. Caricato, X. Li, H. P. Hratchian, A. F. Izmaylov, J. Bloino, G. Zheng, J. L. Sonnenberg, M. Hada, M. Ehara, K. Toyota, R. Fukuda, J. Hasegawa, M. Ishida, T. Nakajima, Y. Honda, O. Kitao, H. Nakai, T. Vreven, J. J. A. Montgomery, J. E. Peralta, F. Ogliaro, M. Bearpark, J. J. Heyd, E. Brothers, K. N. Kudin, V. N. Staroverov, R. Kobayashi, J. Normand, K. Raghavachari, A. Rendell, J. C. Burant, S. S. Iyengar, J. Tomasi, M. Cossi, N. Rega, J. M. Millam, M. Klene, J. E. Knox, J. B. Cross, V. Bakken, C. Adamo, J. Jaramillo, R. Gomperts, R. E. Stratmann, O. Yazyev, A. J. Austin, R. Cammi, C. Pomelli, J. W. Ochterski, R. L. Martin, K. Morokuma, V. G. Zakrzewski, G. A. Voth, P. Salvador, J. J. Dannenberg, S. Dapprich, A. D. Daniels, Ö. Farkas, J. B. Foresman, J. V. Ortiz, J. Cioslowski and D. J. Fox, *Gaussian 09*, Gaussian, Inc., Wallingford CT, 2009.
46 A. D. Becke, *J. Chem. Phys.*, 1993, **98**, 5648–5652.
47 C. Lee, W. Yang and R. G. Parr, *Phys. Rev. B: Condens. Matter Mater. Phys.*, 1988, **37**, 785.
48 W. Kuchle, M. Dolg, H. Stoll and H. Preuss, *J. Chem. Phys.*, 1994, **100**, 7535–7542.
49 X. Y. Cao, M. Dolg and H. Stoll, *J. Chem. Phys.*, 2003, **118**, 487–496.
50 X. Y. Cao and M. Dolg, *THEOCHEM*, 2004, **673**, 203–209.
51 A. Schafer, H. Horn and R. Ahlrichs, *J. Chem. Phys.*, 1992, **97**, 2571–2577.
52 A. Schafer, C. Huber and R. Ahlrichs, *J. Chem. Phys.*, 1994, **100**, 5829–5835.
53 V. S. Bernales, A. V. Marenich, R. Contreras, C. J. Cramer and D. G. Truhlar, *J. Phys. Chem. B*, 2012, **116**, 9122–9129.
54 K. A. Peterson and T. H. Dunning, *J. Chem. Phys.*, 2002, **117**, 10548–10560.
55 T. Lu and F. W. Chen, *J. Comput. Chem.*, 2012, **33**, 580–592.
56 J. Zhang and T. Lu, *Phys. Chem. Chem. Phys.*, 2021, **23**, 20323–20328.
57 S. Grimme, J. Antony, S. Ehrlich and H. Krieg, *J. Chem. Phys.*, 2010, **132**, 154104.
58 W. Humphrey, A. Dalke and K. Schulten, *J. Mol. Graphics*, 1996, **14**, 33–38.
59 M. J. Abraham, T. Murtola, R. Schulz, S. Páll, J. C. Smith, B. Hess and E. Lindahl, *SoftwareX*, 2015, **1–2**, 19–25.
60 A. K. Rappé, C. J. Casewit, K. Colwell, W. A. Goddard III and W. M. Skiff, *J. Am. Chem. Soc.*, 1992, **114**, 10024–10035.
61 G. Garberoglio, *J. Comput. Chem.*, 2012, **33**, 2204–2208.
62 G. Bussi, D. Donadio and M. Parrinello, *J. Chem. Phys.*, 2007, **126**, 014101.
63 R. Parrinello and A. Rahman, *J. Chem. Phys.*, 1981, **52**, 7182–7190.
64 U. Essmann, L. Perera, M. L. Berkowitz, T. Darden, H. Lee and L. G. Pedersen, *J. Chem. Phys.*, 1995, **103**, 8577–8593.
65 F. Neese, *Wiley Interdiscip. Rev.: Comput. Mol. Sci.*, 2012, **2**, 73–78.
66 F. Neese, F. Wennmohs, A. Hansen and U. Becker, *Chem. Phys.*, 2009, **356**, 98–109.
67 J. Zheng, X. Xu and D. G. Truhlar, *Theor. Chem. Acc.*, 2011, **128**, 295–305.
68 A. V. Marenich, C. J. Cramer and D. G. Truhlar, *J. Phys. Chem. B*, 2009, **113**, 6378–6396.
69 B. Chen, J. Liu, H. Wei, Y. Yang, X. Li, S. Peng and Y. Yang, *Chin. Chem. Lett.*, 2022, **33**, 3451–3455.
70 P. R. Danesi, in *Developments in Solvent Extraction*, ed. S. Alegret, Ellis Horwood Ltd, Chichester, UK, 1988, p. 209.
71 C. Z. Wang, J. H. Lan, Y. L. Zhao, Z. F. Chai, Y. Z. Wei and W. Q. Shi, *Inorg. Chem.*, 2013, **52**, 196–203.
72 C. I. Bayly, P. Cieplak, W. Cornell and P. A. Kollman, *J. Phys. Chem.*, 1993, **97**, 10269–10280.
73 T. W. Hayton, *Dalton Trans.*, 2018, **47**, 1003–1009.
74 B. A. D. Neto, A. A. R. Mota, C. C. Gatto, G. Machado, M. Fasciotti, H. C. B. D. Oliveira, D. A. C. Ferreira, O. Bianchi and M. N. Eberlin, *J. Braz. Chem. Soc.*, 2014, **25**, 2280–2294.
75 H. Zhang, H. Liang, J. Wang and K. Li, *Z. Phys. Chem.*, 2007, **221**, 1061–1074.
76 G. Parisi and F. Zamponi, *Rev. Mod. Phys.*, 2010, **82**, 789–845.

77 H. Jin, A. Marmur, O. Ikkala and R. H. A. Ras, *Chem. Sci.*, 2012, **3**, 2526–2529.
78 L. Wang, B. Yuan, J. Lu, S. Tan, F. Liu, L. Yu, Z. He and J. Liu, *Adv. Mater.*, 2016, **28**, 4065–4070.
79 L. Wang, L. Yu, L. Yi, B. Yuan, Y. Hou, X. Meng and J. Liu, *Chem. Commun.*, 2017, **53**, 2347–2350.
80 J. Chen, C. Yang and Z.-S. Mao, *Eur. Phys. J.: Spec. Top.*, 2015, **224**, 389–399.
81 N. Bowden, A. Terfort, J. Carbeck and G. M. Whitesides, *Science*, 1997, **276**, 233–235.
82 M. Bley, B. Siboulet, A. Karmakar, T. Zemb and J.-F. Dufrêche, *J. Colloid Interface Sci.*, 2016, **479**, 106–114.
83 A. Karmakar, M. Duvail, M. Bley, T. Zemb and J.-F. Dufrêche, *Colloids Surf., A*, 2018, **555**, 713–727.
84 M. Špadina, K. Bohinc, T. Zemb and J.-F. Dufrêche, *Langmuir*, 2018, **34**, 10434–10447.
85 M. Špadina, K. Bohinc, T. Zemb and J.-F. Dufrêche, *Langmuir*, 2019, **35**, 3215–3230.
86 M. Špadina and K. Bohinc, *Curr. Opin. Colloid Interface Sci.*, 2020, **46**, 94–113.
87 J. F. Dufrêche and T. Zemb, *Curr. Opin. Colloid Interface Sci.*, 2020, **49**, 133–147.
88 H. Gao, R. Shi, Y. Zhu, H. Qian and Z. Lu, *Chem. Res. Chin. Univ.*, 2022, **38**, 653–670.
89 S. J. Yoon, J. G. Lee, H. Tajima, A. Yamasaki, F. Kiyono, T. Nakazato and H. Tao, *J. Ind. Eng. Chem.*, 2010, **16**, 350–354.
90 J. Luo, C.-Z. Wang, J.-H. Lan, Q.-Y. Wu, Y.-L. Zhao, Z.-F. Chai, C.-M. Nie and W.-Q. Shi, *Dalton Trans.*, 2015, **44**, 3227–3236.
91 G. J. Lumetta, M. J. Wagner and C. D. Carlson, *Solvent Extr. Ion Exch.*, 1996, **14**, 35–60.

